

Two- and Three-Dimensional Simulations of Rayleigh-Taylor Instabilities Using a Coupled Cahn-Hilliard / Navier-Stokes Model

R. Zanella,^{1, a)} G. Tegze,² R. Le Tellier,³ and H. Henry¹

¹⁾Laboratoire PMC, Ecole Polytechnique, CNRS, IP Paris, 91128 Palaiseau Cedex, France

²⁾Wigner Research Centre for Physics, P.O. Box 49, H-1525 Budapest, Hungary

³⁾CEA, DES, IRESNE, DTN, Cadarache, F-13108 Saint Paul-lez-Durance, France

(Dated: December 14, 2020)

We report on two- and three-dimensional numerical simulations of Rayleigh-Taylor instabilities in immiscible fluids. A diffuse-interface model that combines the Cahn-Hilliard equation, governing the evolution of the volume fraction of one fluid, and the Navier-Stokes equations, governing the bulk velocity and pressure, is used. The study is limited to low Atwood numbers owing to the use of the Boussinesq approximation. The code is based on a pseudo-spectral method. A linear analysis is first performed in a two-dimensional case of Rayleigh-Taylor instability to confirm that the model very well captures this phenomenon in the case of inviscid or viscous fluids. One key aspect of this work is that the influence of the thermodynamic parameters related to the Cahn-Hilliard equation (interface thickness and mobility) is quantitatively studied. Three-dimensional results of Rayleigh-Taylor instabilities in viscous fluids are then presented to show the possibilities of this modeling. We observe the effect of the viscosity and the wavelength of an initial single-mode perturbation on the mass transport during the nonlinear regime.

I. INTRODUCTION

The Rayleigh-Taylor instability is a hydrodynamic instability that occurs when two fluids are superimposed with the heavier one on top. If the difference of mass density (simply called density in the following) is sufficient to overcome surface tension, an infinitely small perturbation can destabilize the interface and lead to the progressive interpenetration of the fluid layers, until the heavier fluid has totally dived under the lighter one¹. This instability can be found in many natural phenomena (cosmology, geology, oceanography) or industrial applications (combustion, heat exchangers, mixing, aerosol transport)². The problem has been deeply studied in the case of a single-mode perturbation in order to understand the various stages of the instability. As long as the amplitude of the perturbation is small compared to its wavelength, the growth of the perturbation is exponential³. The growth rate of the instability depends on the excited mode and the densities of the fluids, but also on the surface tension and the viscosity^{4,5}. This regime, said linear because the nonlinear effects are negligible, is followed by a quasi-steady regime. Experiments⁶⁻⁸ revealed that the velocity of the "bubble" of light fluid rising through the heavy fluid reaches a constant value after the exponential growth. Models of terminal velocity taking into account the excited mode and the fluid properties have been theoretically established and confronted to numerical simulations in 2D and 3D⁹⁻¹². After the two first regimes, a re-acceleration regime¹³⁻¹⁶ and a chaotic regime can develop¹⁵. However, most of the aforementioned work is focused on the high Reynolds number regime where

inertia is dominant and little is known on the low or intermediate Reynolds number regime.

For this purpose, we have used a diffuse-interface model and more precisely a coupled Cahn-Hilliard / Navier-Stokes model (CHNS model). Diffuse-interface models rely on the use of a transport equation for an order parameter that indicates in which phase each point of space is and that smoothly varies between the phases¹⁷. As a result, the interface is tracked implicitly as an iso-surface of the order parameter. The boundary conditions at the interface are then imposed through a proper coupling between the transport equation of the order parameter and the flow equations. In the case of the CHNS model, the transport equation is the Cahn-Hilliard equation^{18,19} and it can be coupled in a thermodynamically consistent way with the Navier-Stokes equations so that capillary effects are well described. However, non-hydrodynamic parameters related to the Cahn-Hilliard equation appear in the modeling: the interface thickness at thermodynamic equilibrium and the mobility. The use of a Cahn-Hilliard model in practical situations involves the upscaling of the interface thickness from actual sizes to sizes compatible with numerical simulations (a small but not too small fraction of the characteristic length-scale of the system). The effects of this upscaling and how to perform it by appropriately choosing the interface thickness and the mobility is a delicate problem. A recipe has recently been proposed in Ref. 20, suggesting a scaling between the mobility and the ratio of the interface thickness and the characteristic length of the problem.

The CHNS model has already been used to simulate Rayleigh-Taylor instabilities in various studies. In Ref. 21, the model was used in two dimensions and shown to give fairly accurate results in the linear and weakly nonlinear regimes for viscous and non viscous fluids. However, the convergence of the model with respect to

^{a)}Electronic mail: zanella.raphael@gmail.com

the thermodynamic parameters (interface thickness and mobility) was not presented. In Refs. 22 and 23, two- and three-dimensional simulations were performed for physical parameters corresponding to moderate Atwood number and relatively high Reynolds number (but no surface tension). The simulations showed the ability of the model to qualitatively reproduce the expected behavior but the influence of the Péclet number (related to the mobility) was only qualitatively discussed in Ref. 22. Ref. 24 focused on the chaotic regime at high Reynolds number. However, no discussion of the role of the thermodynamic parameters was provided. In Ref. 25, the Rayleigh-Taylor instability in a torus was used as a qualitative test of a finite element approach. No physical explanation was given regarding the thermodynamic parameters. Ref. 26 addressed the particular case of Rayleigh-Taylor instabilities under the influence of an electric field. The influence of the thermodynamic parameters was nevertheless not studied. The interplay of flow and diffusion during the mixing of miscible fluids assisted by a Rayleigh-Taylor instability was explored in Ref. 27. In this case, contrary to the case treated in Ref. 20, the diffusive mass transport must not be neglected. Hence, while many studies show that the use of the CHNS model can well reproduce the Rayleigh-Taylor instability both in 2D and 3D, the thermodynamic parameters are usually considered as free parameters of the model. The way they are chosen is not always explained and if so, their influence on the results is not quantitatively assessed. The lack of convergence studies makes it difficult to use the CHNS model in practical applications where some accuracy and a good estimate of the error is needed.

In this paper, we show the ability of the CHNS model to capture the evolution of Rayleigh-Taylor instabilities, highlighting the role of the thermodynamic parameters on the convergence of the model. In the same spirit as a work performed in a different multiphase flow context²⁸, we compare our convergence results with the scaling of Ref. 20. The study is limited to immiscible fluids in the low Atwood number limit where the difference of the fluid densities is small compared to their sum (the Boussinesq approximation is used). We first present the governing equations, highlighting the specificity of this diffuse-interface model compared to a sharp interface model. We then describe the pseudo-spectral numerical method that we use. We then show the validation of the model on two-dimensional Rayleigh-Taylor instabilities in the linear regime, based on the theoretical growth rates, and discuss the impact of the thermodynamic parameters on the accuracy of the results. We finally report results on three-dimensional Rayleigh-Taylor instabilities in the nonlinear regime in viscous fluids (low Reynolds number / Stokes regime or intermediate Reynolds number configurations: $R_e \sim 10^{-2}$ to 10^2). We observe here the influence of the viscosity and of the wavelength of an initial single-mode perturbation on the mass transport, and discuss briefly the transition toward the high Reynolds number regime.

II. GOVERNING EQUATIONS

In this section, we briefly present the Cahn-Hilliard model considered (in the absence of fluid flow), then detail how it is coupled to the Navier-Stokes equations to obtain the CHNS model and finally discuss the considered physical properties.

A. Cahn-Hilliard model (in the absence of fluid flow)

The Cahn-Hilliard model^{18,19} originally aimed at describing the phase separation of two chemical species that separate into two homogeneous phases and was inspired by earlier works of van der Waals on phase separation. For this purpose, a concentration field is introduced. Here, the considered system of two immiscible fluids is seen as a system of two fluids 1 and 2 with miscibility gap and this concentration field, denoted by c , represents the molar fraction of fluid 2. In the absence of fluid flow, the concentration field obeys the simple diffusion equation

$$\partial_t c = M \Delta \mu, \quad (1)$$

where M is the mobility and μ the diffusion potential (the difference between the chemical potentials of fluids 2 and 1: $\mu = \mu_2 - \mu_1$), which derives from a free energy functional:

$$\mu = \frac{\delta \mathcal{F}}{\delta c}, \quad (2)$$

$$\mathcal{F} = \int \left(f_0(c) + \frac{\epsilon}{2} (\nabla c)^2 \right) dV, \quad (3)$$

where f_0 is the free energy by unit volume of an homogeneous system and ϵ a positive constant. Note that a constant molar volume is assumed. In our case, f_0 is of the form

$$f_0(c) = A c^2 (1 - c)^2, \quad (4)$$

where A is a positive constant. A and ϵ are model parameters that relate to parameters with more physical meaning, as shown next. With this system of equations, one can prove that the thermodynamic equilibrium solution is a system separated into two domains with concentrations 0 and 1 (the two minima of f_0). This is appropriate to describe immiscible fluids because it means that the phases are composed of fluid 1 or 2 exclusively. Assuming an infinite domain, the concentration profile at thermodynamic equilibrium is of the form¹⁸

$$c(X) = \frac{1}{2} \left(1 + \tanh \left(\frac{X}{w_{int}} \right) \right), \quad (5)$$

where X is the position on an axis perpendicular to the interface and such that the interface is at $X = 0$ and

$$w_{int} = \sqrt{\frac{2\epsilon}{A}} \quad (6)$$

can be defined as the interface thickness. The interfacial free energy of the system is defined by¹⁸

$$\gamma = \int_0^1 \sqrt{2\epsilon f_0(c)} dc \quad (7)$$

at thermodynamic equilibrium. This quantity corresponds to the surface tension between the fluids. By replacing f_0 with Eq. (4) and integrating, we have

$$\gamma = \sqrt{\frac{A\epsilon}{18}}. \quad (8)$$

One can note that Eqs. (6) and (8) can be easily reversed to obtain:

$$A = \frac{6\gamma}{w_{int}}, \quad (9)$$

$$\epsilon = 3w_{int}\gamma. \quad (10)$$

B. Coupled Cahn-Hilliard / Navier-Stokes model

We now describe the coupled CHNS model that describes the evolution of the concentration, velocity and pressure fields in the presence of fluid flow. This model is similar to the ones used in previous work^{21–23,25,29}. The Cahn-Hilliard equation in Eq. (1) is modified to take into account the effect of the fluid flow through the use of a convective term. It writes then

$$\partial_t c + \mathbf{v} \cdot \nabla c = M \Delta \mu, \quad (11)$$

where \mathbf{v} is the velocity.

The Navier-Stokes equations (under the Boussinesq approximation) are then extended with a source term to take into account the capillary force:

$$\begin{aligned} \partial_t \mathbf{v} + \nabla \cdot (\mathbf{v} \otimes \mathbf{v}) + \frac{1}{\rho_1} \nabla p - \nabla \cdot (2\nu(c) \nabla^s \mathbf{v}) = \\ - \frac{1}{\rho_1} \left(c - \frac{1}{2} \right) \nabla \mu + \frac{\rho(c)}{\rho_1} \mathbf{g}, \end{aligned} \quad (12)$$

$$\nabla \cdot \mathbf{v} = 0, \quad (13)$$

where p is the pressure, ν the kinematic viscosity, $\nabla^s \mathbf{v}$ the shear rate tensor defined by

$$\nabla^s \mathbf{v} = \frac{1}{2} (\nabla \mathbf{v} + (\nabla \mathbf{v})^T), \quad (14)$$

ρ_i the density of fluid i and \mathbf{g} the gravity. The term associated to the diffusion potential in Eq. (12) represents the capillary force and derives from a stress tensor analogous to that of Korteweg¹⁷. The dynamic viscosity is assumed to depend linearly on c so that

$$\nu(c) = \frac{\eta_1 + (\eta_2 - \eta_1)c}{\rho_1}, \quad (15)$$

where η_i is the dynamic viscosity of fluid i . The density is also assumed to depend linearly on c :

$$\rho(c) = \rho_1 + (\rho_2 - \rho_1)c. \quad (16)$$

C. Physical properties

In the whole work, the following densities and surface tension are considered: $\rho_1 = 1000 \text{ kg} \cdot \text{m}^{-3}$, $\rho_2 = 1010 \text{ kg} \cdot \text{m}^{-3}$ and $\gamma = 0.05 \text{ N} \cdot \text{m}^{-1}$. These properties are close to those of water. The viscosities are varied and are taken equal to 0 when considering perfect fluids. The standard acceleration of gravity is $g = 9.80665 \text{ m} \cdot \text{s}^{-2}$.

Regarding the interface thickness and the mobility, we use various values detailed later. We nevertheless find it interesting to briefly discuss here the way these parameters, that are not directly related to quantities usually used to describe fluid flows, should be chosen. Let us first discuss the choice of the interface thickness. In actual systems, the interface thickness is of the order of a nanometer. From a numerical point of view, simultaneously resolving scales ranging from nanometers to meters is clearly out of reach. We can nevertheless expect that the difference between a sharp-interface model and a diffuse-interface model will vanish when w_{int}/L , where L is the characteristic length scale of the problem, tends to zero²⁰. Therefore, w_{int} should be taken small compared to the characteristic length scale of the problem.

As also explained in Ref. 20, the choice of the value of the mobility, which can also be considered as a kinetic parameter, involves to take into account two effects of the diffusion. At the scale of the interface between the phases, it restores the thermodynamic equilibrium profile that has been deformed by advection. This effect is needed since the capillary force is function of the concentration profile and the actual surface tension is retrieved only if the concentration profile of the interface is the equilibrium profile. Otherwise, the surface tension is overestimated. On the macroscopic scale, the diffusion process tends to smoothen the interface through the diffusive transport of matter from high curvature regions to low curvature regions. This induces a motion of the interface whose velocity is function of the mobility. This velocity in actual systems is negligible compared to the fluid flows and M must therefore be chosen accordingly in the model. As a result, the choice of M is a compromise between a sufficiently fast diffusive process (compared to fluid flow), that ensures that the interface profile stays the equilibrium profile, and a sufficiently slow one, that avoids the appearance of a significant interface motion due to diffusion and not fluid flow. We find it important to mention that to satisfy these two requirements a sufficient scale separation between the interface thickness and the macroscopic length scale is needed.

III. NUMERICAL METHOD

The model equations are solved using a pseudo-spectral method that has already been used in Refs. 30 and 31. It relies on the use of the Fourier transform in a periodic domain along directions x , y and z . The solution fields are assumed periodic of periods $N_x \Delta x = L_x$

in the x direction, $N_y \Delta x = L_y$ in the y direction and $N_z \Delta x = L_z$ in the z direction, where $\Delta x > 0$ is the mesh size and $N_x \in \mathbb{N}$ (resp. $N_y/N_z \in \mathbb{N}$) is the number of Fourier modes used in the x (resp. y/z) direction. The solving consists in computing the $N_x \times N_y \times N_z$ Fourier coefficients associated to the solution fields at every time $t^n = n\tau$, where $n \geq 0$ and $\tau > 0$ is the time step. The nonlinear terms of the governing equations are treated explicitly while the linear terms are treated implicitly using a simple first order Euler time stepping scheme. The incompressibility condition is imposed through a standard Helmholtz projection method. Owing to the explicit treatment of the nonlinear terms, the time step is limited by the Courant-Friedrich-Lewy condition.

We use sufficiently high domains so that the interfaces at the top and bottom boundaries are remote from the unstable interface and do not affect the development of the instability, up to the accuracy of our computations.

IV. LINEAR ANALYSIS IN TWO DIMENSIONS

As mentioned above, a better understanding of the quality of the approximation of the sharp-interface multiphase flow equations by the CHNS model is needed. To this purpose, we consider the onset of the Rayleigh-Taylor instability. In this case, the dispersion relation of the instability is known analytically in the case of perfect fluids and is known with good accuracy in the case of viscous fluids. In this section, we first describe the problem setup, focusing on the initial condition and on the method used to extract the growth rate. We then present numerical results in the case of perfect fluids, which allows us to discuss the convergence of the model regarding the thermodynamic parameters. We finally present numerical results obtained in the case of viscous fluids.

A. Problem setup

The dispersion relation is established in a system that is a $[0, L_x] \times [0, L_z]$ domain where the gravity field is oriented along the z axis: $\mathbf{g} = -g\mathbf{e}_z$, $g > 0$. An initial perturbation of the horizontal interface (where the heavy fluid is above the lighter one)

$$\Delta h(t=0) = \zeta_0 \cos(kx), \quad k > 0, \quad (17)$$

will grow exponentially in the earliest times:

$$\Delta h(t) = \zeta(t) \cos(kx), \quad \zeta(t) = \zeta_0 e^{\alpha t}, \quad (18)$$

where α is the growth rate given by

$$\alpha = \sqrt{\frac{\rho_2 - \rho_1}{2\rho_1} gk - \frac{\gamma}{2\rho_1} k^3} \quad (19)$$

in the case of perfect fluids, or obtained by solving an equation detailed in Appendix A in the case of viscous fluids, under the condition that the wavenumber k is smaller

than a critical wavenumber k_c given by

$$k_c = \sqrt{\frac{(\rho_2 - \rho_1)g}{\gamma}}. \quad (20)$$

The formula in Eq. (19) is adapted from the classical one (see Ref. 4, p. 435, Eq. (51) for instance), where the denominators $2\rho_1$ are replaced by $\rho_1 + \rho_2$, owing to the use of the Boussinesq approximation. With the considered physical parameters, we have $k_c \approx 44 \text{ m}^{-1}$.

The aim of this study is to compute the growth rates of single-mode perturbations with various wavelengths and to confront them with the theoretical growth rates. We therefore use as an initial condition what we consider a good approximation of a single mode (transposed in the framework of a diffuse-interface model). In this test, we only consider the unstable wavenumbers

$$k_0 = \frac{2I_0\pi}{L}, \quad 1 \leq I_0 \leq E \left(\frac{k_c L}{2\pi} \right), \quad (21)$$

where $L = 1 \text{ m}$ is the maximum considered wavelength. The horizontal domain length is set to one wavelength of the perturbation: $L_x = \lambda_0 = 2\pi/k_0 = L/I_0$. The vertical dimension is $L_z = 2L_x$. We initialize the concentration with

$$c_0(x, z) = \begin{cases} \frac{1}{2} \left(1 - \tanh \left(\frac{z}{w_{int}} \right) \right) & \text{if } 0 \leq z < L_z/4, \\ \frac{1}{2} \left(1 + \tanh \left(\frac{z - \frac{L_z}{2} - \zeta_0 \cos(k_0 x)}{w_{int}} \right) \right) & \text{if } L_z/4 \leq z < 3L_z/4, \\ \frac{1}{2} \left(1 - \tanh \left(\frac{z - L_z}{w_{int}} \right) \right) & \text{if } 3L_z/4 \leq z \leq L_z, \end{cases} \quad (22)$$

where $\zeta_0 = 0.5 \times 10^{-4} \lambda_0$ introduces a very small perturbation, and the velocity with

$$\mathbf{v}_0(x, z) = \begin{cases} \alpha \zeta_0 e^{k_0 z} (-\sin(k_0 x) \mathbf{e}_x + \cos(k_0 x) \mathbf{e}_z) & \text{if } 0 \leq z < L_z/2, \\ \alpha \zeta_0 e^{-k_0 z} (\sin(k_0 x) \mathbf{e}_x + \cos(k_0 x) \mathbf{e}_z) & \text{if } L_z/2 \leq z \leq L_z, \end{cases} \quad (23)$$

following the analytical solution.

We then monitor the rise, with respect to $n \geq 0$, of the kinetic energy per unit volume carried by every mode I_0 ,

$$E_{k,0}(t^n) \approx \frac{1}{2} \rho_1 \sum_{K=-N_z/2}^{N_z/2} (|v_{x,I_0 0 K}^n|^2 + |v_{z,I_0 0 K}^n|^2), \quad (24)$$

where $v_{x,I_0 0 K}^n$ and $v_{z,I_0 0 K}^n$ are the $(I_0, 0, K)$ Fourier coefficients at t^n of the velocity components v_x and v_z , respectively. $E_{k,0}(t)$ should grow as $e^{2\alpha t}$ owing to the power 2

over the velocity coefficients. In order to compute the growth rate we consider the evolution of this quantity between an initial state where the amplitude of the perturbation is $2\zeta_0 = \lambda_0/10^4$ and a final state where it is $2\zeta(t_{1/10}) \approx \lambda_0/10$, i.e., for which the nonlinear effects are still negligible. Assuming that the analytical prediction of the velocity holds, this final state corresponds to a time

$$t_{1/10} = \frac{1}{\alpha} \ln \left(\frac{\lambda_0}{20\zeta_0} \right). \quad (25)$$

Hence, we can follow the growth of the perturbation amplitude over three orders of magnitude in the linear regime.

B. Interface thickness and mobility

We now detail how the thermodynamic parameters that have not been defined earlier (interface thickness and mobility) are determined. The interface thickness should be small compared to the characteristic size of the perturbation in order to approach the sharp interface limit. According to the results of the convergence study on this parameter (see Fig. 4a) and to keep the computational cost reasonable, here we set $w_{int} = \lambda_0/128$ (this value is only changed when performing the convergence study). We therefore use a Cahn number (ratio of the interface thickness and the characteristic lengthscale)

$$C_n = \frac{w_{int}}{\lambda_0} = \frac{1}{128}. \quad (26)$$

The convection needs to dominate the diffusion at the macroscopic scale for the convective flow to develop. This requirement is expressed by a strong Péclet number defined as

$$P_e = \frac{v_l \lambda_0 w_{int}}{M\gamma}, \quad (27)$$

where v_l is the characteristic velocity. However, this number must be not too large so that diffusion is dominant at the interface scale and local thermodynamic equilibrium is enforced at any time. Once again based on the analytical velocity, we can estimate that the maximum velocity (at $t_{1/10}$) is

$$v_l = \frac{\lambda_0 \alpha}{20}. \quad (28)$$

We set M such that $P_e = 1000$ (this value is only changed when performing a convergence study on this parameter for Fig. 4b).

These choices are justified by the convergence studies presented in Fig. 4. Note that these studies are performed with a finer mesh than the rest due to the use of smaller values of w_{int} .

C. Numerical parameters

Since the interface must be resolved, we use a grid spacing such that there are 4 cells in the interface thickness ($\Delta x = w_{int}/4$), which leads to $N_x = 512$ and $N_z = 1024$ (this is only changed when performing the convergence study for Fig. 4). N_y has been set to 1 because we consider the two-dimensional case. We then define τ to at least satisfy the condition

$$\frac{v_l \tau}{\Delta x} \leq 0.25. \quad (29)$$

Much smaller values are used to reach convergence for the largest I_0 cases.

D. Results in the case of non viscous fluids

First, in order to illustrate quantitatively the development of the instability, we have performed a simulation that goes clearly beyond the linear regime ($t > t_{1/10}$) for $I_0 = 1$. In the later moments, since the velocity is much greater than v_l , a time step much smaller than that obtained by following Section IV C is needed. We also use a tiny viscosity $\eta = 10^{-3} \text{ Pa} \cdot \text{s}$ in this particular case, and beyond the linear regime, to help dissipating the momentum and to avoid too strong concentration gradients. During this simulation, the initial perturbation grows exponentially with time and after an initial regime where the initial perturbation sine wave is amplified, there is the formation of a spike of heavy fluid falling in the light fluid while there is a bubble of light fluid rising in the heavy fluid. This behavior is illustrated in Fig. 1 where a series of color plots representing the interface between the two phases and the flow speed is shown.

Hence, the model is able to reproduce qualitatively the phenomenon observed during the Rayleigh-Taylor instability. We now turn to a more quantitative analysis where η is set to zero. To this purpose, we determine the growth rate of the instability (in the linear regime) by fitting linearly the curve of $\log(E_{k,0}(t))$ between

$$t_{1/1000} = \frac{1}{\alpha} \ln \left(\frac{\lambda_0}{2000\zeta_0} \right) \quad (30)$$

and

$$t_{1/100} = \frac{1}{\alpha} \ln \left(\frac{\lambda_0}{200\zeta_0} \right), \quad (31)$$

the theoretical times needed for the perturbation amplitude to reach one thousandth and one hundredth of the wavelength, respectively. The estimated growth rate is the half of the slope of the fitting curve. A typical evolution of $E_{k,0}(t)$ and of the fitting curve (that of the case $I_0 = 1$) is shown in Fig. 2, which shows that the fit is remarkably good. In this case, the fitting is performed between $t_{1/1000} \approx 4.2 \text{ s}$ and $t_{1/100} \approx 8.4 \text{ s}$. The fact that the linear regime is observed without ambiguity from the

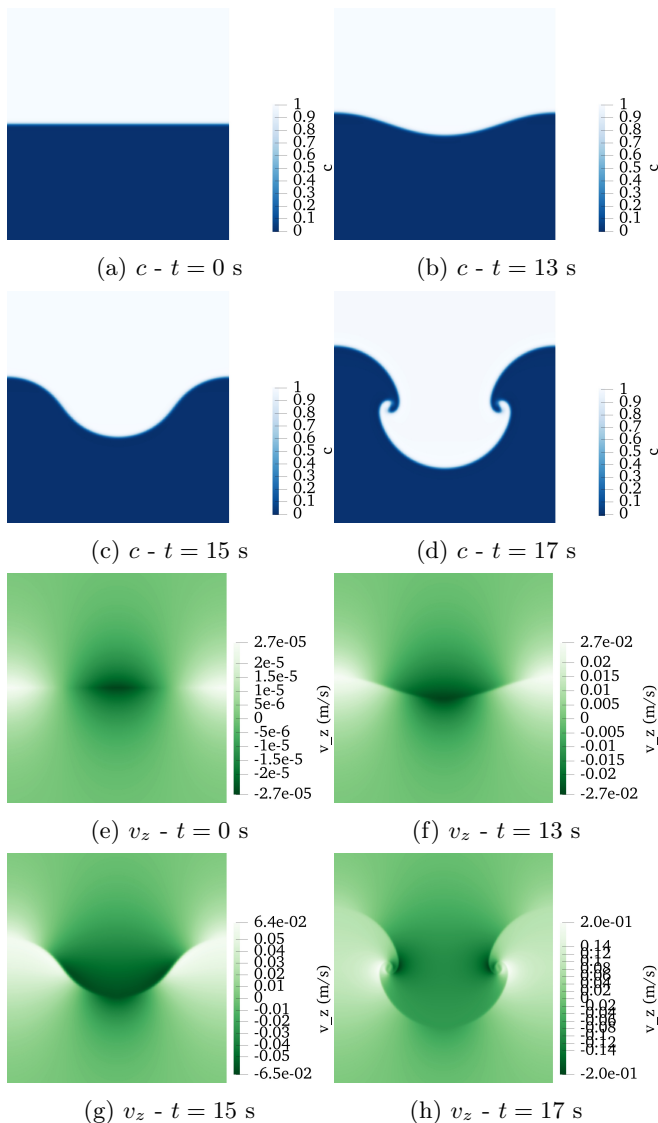


Figure 1: Concentration and vertical velocity fields during the linear regime ($t < t_{1/10} \approx 12.6$ s) and the nonlinear regime of the instability ($t > t_{1/10}$) for $I_0 = 1$.

start is due to our choice of initial condition where the velocity field is not set to zero but to the analytical solution.

From this procedure we are able to extract the growth rate for different values of the wavelength and the obtained values are plotted in Fig. 3 together with the theoretical growth rate. The wavenumber is normalized by the critical wavenumber, while the growth rate is normalized by the maximum growth rate α_{max} , which is obtained for the most unstable wavenumber

$$k_{max} = \frac{1}{\sqrt{3}}k_c. \quad (32)$$

One can see that the match between the numerical points and the theoretical curve is very good. This indicates that, as already discussed in Refs. 21 and 22 for instance,

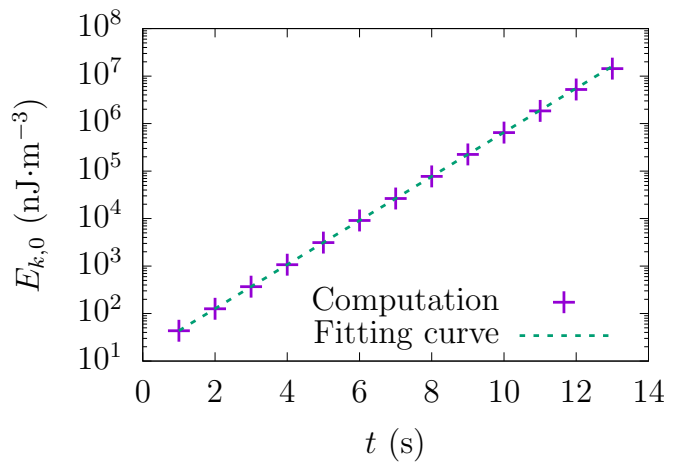


Figure 2: Plot of the kinetic energy (using a log scale) carried by mode I_0 as a function of time (using a linear scale). The very good match between the data points and the linear fit indicates that the system is still in the linear regime characterized by an exponential growth.

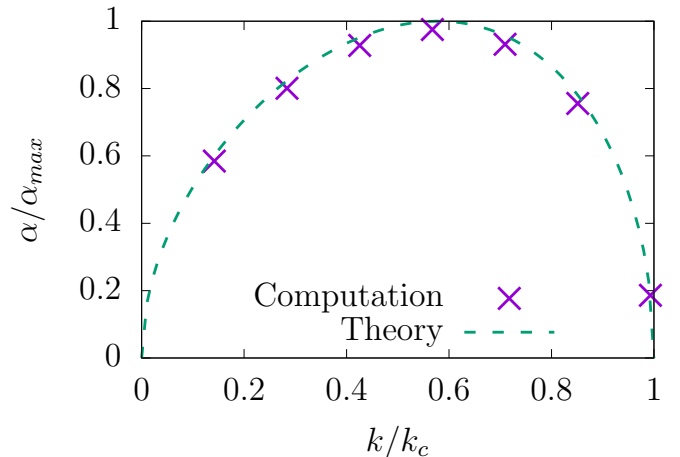
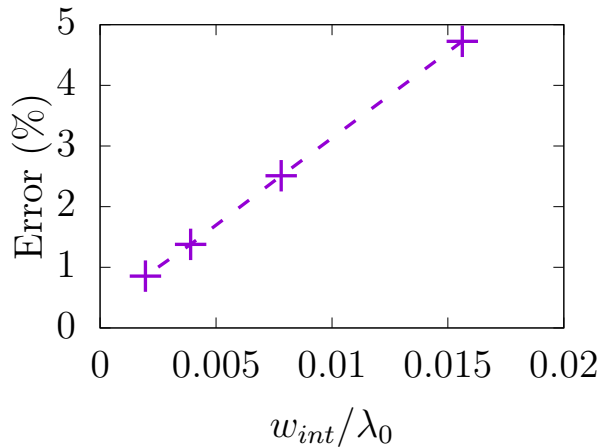


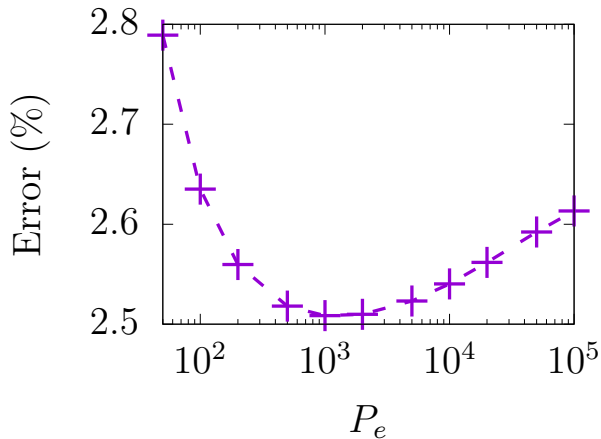
Figure 3: Theoretical versus computed growth rates in the case of perfect fluids. Here, $\alpha_{max} \approx 0.91$ s $^{-1}$.

the CHNS model can quantitatively well reproduce the Rayleigh-Taylor instability in the case of perfect fluids.

However, there remains a small model-related error. We will now discuss more thoroughly the origin of this error and to what extent it can be controlled. The thermodynamic model is fully specified by three parameters: the surface tension, the interface thickness and the mobility. The surface tension is determined by the physics of the problem and is therefore not a model parameter. The interface thickness and the mobility are model parameters and can be fixed freely (at least in the case of the description of the Rayleigh-Taylor instability). Let us first discuss the interface thickness effect. Due to the non-zero interface thickness in our model, the numerical solution does not exactly match the analytical one, in particular regarding the growth rate. We plot in Fig. 4a the relative error on the growth rate (case $I_0 = 1$) as



(a) Interface thickness effect



(b) Péclet number effect

Figure 4: Influence of the interface thickness and the Péclet number on the error on the growth rate $|(\alpha_{comp} - \alpha_{th})/\alpha_{th}|$ (case $I_0 = 1$). The cross marks represent computational results. The dashed line is a guide for the eye.

a function of the Cahn number. The mobility is such that the Péclet number is always $P_e = 1000$. One can see that the error linearly decreases with this ratio. This therefore confirms that the interface thickness must be as small as possible so that the effects of the diffuse interface are limited. However, one can also see that the linear fit does not reach exactly zero when C_n goes to 0. From the analysis²⁰, this is due to the fact that here the Péclet number is taken constant.

Let us now discuss the mobility effect. On the one hand, for a given interface thickness and in the limit of large mobilities, the growth of the instability is counterbalanced by the diffusion, which results in an underestimation of the growth rate. On the other hand, in the limit of low mobilities, the diffusion cannot restore the proper interface profile, which results in an overestimation of the surface tension and therefore in an underestimation of the growth rate. This is illustrated in Fig. 4b,

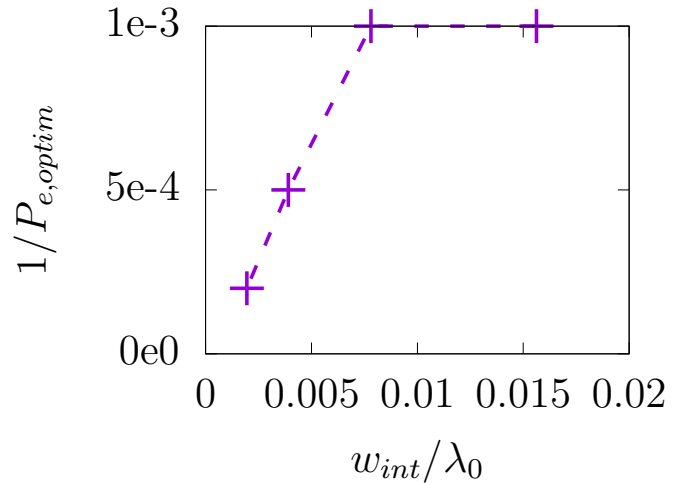


Figure 5: Inverse of the optimal Péclet number as a function of the Cahn number.

where the relative error on the growth rate (case $I_0 = 1$) is plotted as a function of the Péclet number. The interface thickness is always $\lambda_0/128$. Recall that the mobility is inversely proportional to the Péclet number. One can see that the error decreases with the mobility until a certain value ($P_e \leq 1000$) and that it then increases when the mobility is further reduced ($P_e \geq 1000$). This study confirms that the mobility must be small enough to avoid that diffusive transport counterbalances the instability mechanism, but also large enough to allow the restoration of the thermodynamic equilibrium profile at the interface by diffusive process. These two plots also show that an optimal value of the mobility exists for a given interface thickness (here it corresponds to $P_e = 1000$ approximately).

The influence of the Péclet number on the accuracy of the result is studied for various values of the interface thickness. Every tested value of w_{int} presents an optimal value of P_e . We present the inverse of the optimal Péclet number as a function of the Cahn number in Fig. 5. We can see that $1/P_{e,optim}$ is proportional to C_n when C_n tends to 0, which is in good agreement with the theoretical work²⁰. In Ref. 20, their optimal dimensionless mobility is predicted to be proportional to the square of the Cahn number but the ratio of the Cahn number and the dimensionless mobility is the Péclet number so it is equivalent.

E. Results in the case of viscous fluids

We now take advantage of the versatility of the model to study the effects of varying the viscosities of both fluids and compare the numerical results with the predicted growth rates presented in Ref. 5. First, we consider the case where both fluids share the same viscosity, which is such that there is a significant departure from the perfect fluid case ($\eta_1 = \eta_2 \geq 0.1 \text{ Pa} \cdot \text{s}$). We plot in Fig. 6 the

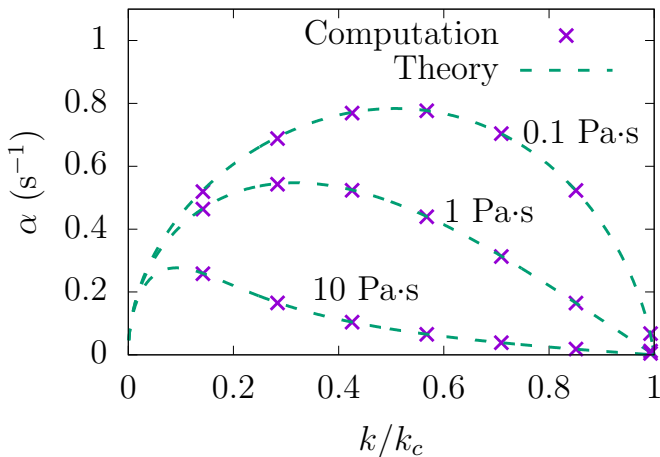


Figure 6: Theoretical versus computed growth rates in the case of viscous fluids. Both fluids have the same viscosity.

computed growth rate as a function of the normalized wavenumber for different values of the viscosity together with the predictions of Ref. 5 (details of the calculation are recalled in Appendix A). As expected (see Ref. 4, p. 447), the wavenumber domain for which the two fluid system is unstable is independent of the viscosity (for a given surface tension), which translates into the fact that the curves tend toward a zero growth rate for the same value of the wavenumber as in the inviscid case ($k = k_c$). In addition, the agreement between our computations and the theoretical predictions is very good.

We show that the agreement is excellent in Fig. 7, where we plot the relative difference between the growth rate for perfect fluids and the growth rate for viscous fluids. For small values of the wavenumber, the relative difference is small and increases with k . This would be expected because of the fact that energy dissipation is higher at high wavenumber. The computed slopes close to $k = 0$ are in very good agreement with theoretical predictions. At values close to $k = k_c$, the theoretical curves have the property that they all converge toward 1 (while the growth rates converge all toward 0 in $k = k_c$). This behavior is (as can be seen) very well reproduced by the numerical points. Similar results were presented in Ref. 21. However, the comparison was not as compelling since it was limited to the bounds on the growth rates given by Ref. 5. The exact growth rates (which can be numerically obtained by solving an equation, see Appendix A) were not considered.

We now consider that the lower fluid has a fixed viscosity ($\eta_1 = 1 \text{ Pa} \cdot \text{s}$) while the viscosity of the upper fluid is varied and can take a different value ($\eta_2 = 0.1, 1$ or $10 \text{ Pa} \cdot \text{s}$). The computed versus theoretical growth rates for different values of the viscosities are plotted as a function of the normalized wavenumber in Fig. 8. Again, the agreement between our computations and the theoretical predictions is very good in this case (not treated

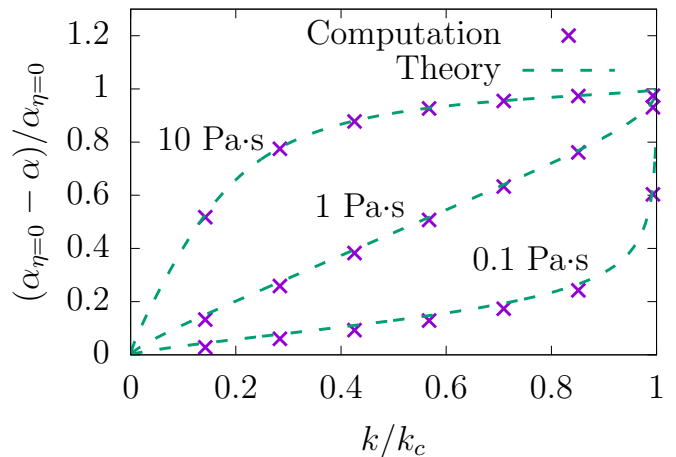


Figure 7: Relative difference between the growth rate for perfect fluids $\alpha_{\eta=0}$ and the growth rate for viscous fluids (with the same viscosity).

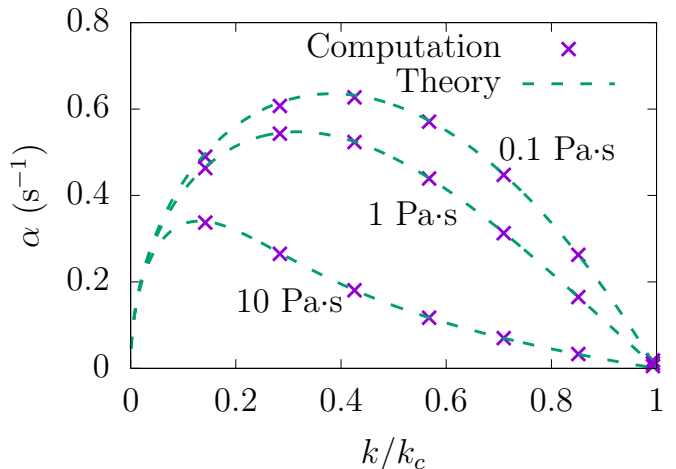


Figure 8: Theoretical versus computed growth rates in the case of viscous fluids. The viscosity of the lower fluid stays fixed at $\eta_1 = 1 \text{ Pa} \cdot \text{s}$ while that of the upper fluid varies.

in Ref. 21).

From this study, it is clear that the CHNS model reproduces quantitatively well the Rayleigh-Taylor instability in the viscous case as well.

V. STUDY OF THE NONLINEAR REGIME IN THREE DIMENSIONS

We extend the simulations performed in the previous section with three-dimensional simulations of the Rayleigh-Taylor instability in the nonlinear regime. In particular, we study the effect of the perturbation wavelength and of the viscosity on the mass transport in a low-intermediate Reynolds number regime where viscous effects are significant and for which a steady regime is

observed. We also briefly discuss the departure from the steady state when the Reynolds number is increased. In Ref. 23, three-dimensional simulations in the nonlinear regime were also performed with a similar model (but no surface tension). Here, we take here into account surface tension and perform long-time simulations in high computational domains where the constant bubble velocity and possibly a reacceleration stage can clearly be observed. We believe that these results will supplement existing ones, so that the CHNS model is shown to be able to well reproduce complex multiphase flows. As in the previous section, we first present the problem setup and then the numerical results.

A. Problem setup

The system is a $[0, L_x] \times [0, L_y] \times [0, L_z]$ domain where the gravity field is still oriented along the z axis: $\mathbf{g} = -g\mathbf{e}_z$, $g > 0$. L_x is chosen to be equal to L_y and ranges between $\approx \lambda_c$ and $7\lambda_c$, where

$$\lambda_c = \frac{2\pi}{k_c}, \quad (33)$$

with k_c defined in Eq. (20), is the critical wavelength. With the considered physical parameters, we have $\lambda_c \approx 0.14$ m. The vertical dimension is taken sufficiently large compared to the horizontal dimension to observe the nonlinear regime ($L_z \geq 4L_x$). L_z is chosen between $\approx 15\lambda_c$ and $60\lambda_c$. We initialize the concentration with

$$c_0(x, y, z) = \begin{cases} \frac{1}{2} \left(1 - \tanh \left(\frac{z}{w_{int}} \right) \right) & \text{if } 0 \leq z < L_z/4 \\ \frac{1}{2} \left(1 + \tanh \left(\frac{z - \frac{L_z}{2} - \zeta_0 p(x, y)}{w_{int}} \right) \right) & \text{if } L_z/4 \leq z < 3L_z/4, \\ \frac{1}{2} \left(1 - \tanh \left(\frac{z - L_z}{w_{int}} \right) \right) & \text{if } 3L_z/4 \leq z \leq L_z, \end{cases} \quad (34)$$

where ζ_0 is taken small compared to the wavelength and

$$p(x, y) = \cos(k_0 x) + \cos(k_0 y), \quad (35)$$

with $k_0 = 2\pi/L_x$. Hence, the initial condition is chosen so that a single wavelength of the initial perturbation is present in the simulation box ($L_x = L_y = \lambda_0$). The velocity is set to zero initially.

B. Interface thickness and mobility

In this case, these parameters are the same for every considered wavelength. We use a small value of the interface thickness $w_{int} = L/128$, with $L = 1$ m, compared

to the considered wavelengths (L is the maximum considered wavelength). For $\lambda_0 \approx 1.32\lambda_c$, the smallest wavelength considered here, we have $w_{int}/\lambda_0 \approx 0.042$, which would imply an error on the growth rate of $\approx 10 - 15\%$ (extrapolation based on Fig. 4a).

The mobility is set to a small value $M \approx 8.43 \times 10^{-6} \text{ J}^{-1} \cdot \text{m}^5 \cdot \text{s}^{-1}$ that leads to a Péclet number during the nonlinear regime in the range $[5, 2000]$ according to *a posteriori* estimates with a reference fluid velocity being the bubble tip velocity v_b (the velocity of the highest point of the interface).

C. Numerical parameters

We choose here to use 2 cells in the interface thickness ($\Delta x = w_{int}/2$), which leads to various values of N_x (and N_y which takes the same value) between 48 and 256 depending on λ_0 . N_z goes from 512 to 2048 depending on L_z . The time step is taken small enough to reach convergence ($10^{-3} \text{ s} \leq \tau \leq 0.1 \text{ s}$ depending on the viscosity).

D. Results

Before describing the results, we find it necessary to mention that in our simulations the heavy and light fluids are perfectly symmetric in the sense that their motion is symmetric with respect to the mid-plane of the simulation setup (the initial position of the interface). We have chosen to focus on the motion of the light fluid. However, one should keep in mind that the perfectly symmetric motion of the heavy fluid is always present.

With the chosen parameters and the initial condition defined by Eq. (35), the mode of the initial perturbation is always the one dominating during both the linear and the nonlinear regimes of the instability. In the case of small systems, $L_x < 2\lambda_c$, this is obvious since the harmonics of the initial perturbation correspond to linearly stable modes. In the case of larger systems, either the perturbation was growing faster than its harmonics (most cases) or the initial contribution of the harmonics was sufficiently small to not outgrow the excited mode. As a result, all of what will be presented in the following has been obtained through the growth of a single mode, or more precisely, of two modes oriented along the x axis and the y axis that share the same wavelength.

In the whole section, the dynamic viscosities of both fluids are the same and we note it η . The patterns that form during the nonlinear stage are similar to the one presented in Fig. 9, obtained for one of the tested cases ($\lambda_0 \approx 1.76\lambda_c$, $\eta = 2 \text{ Pa} \cdot \text{s}$), that is the growth of a bubble of light fluid followed by a narrower fluid filament rising in the heavy fluid. In this case, the Reynolds number, which can be defined as

$$Re = \frac{\rho_1 \max_t(v_b(t))\lambda_0}{\eta}, \quad (36)$$

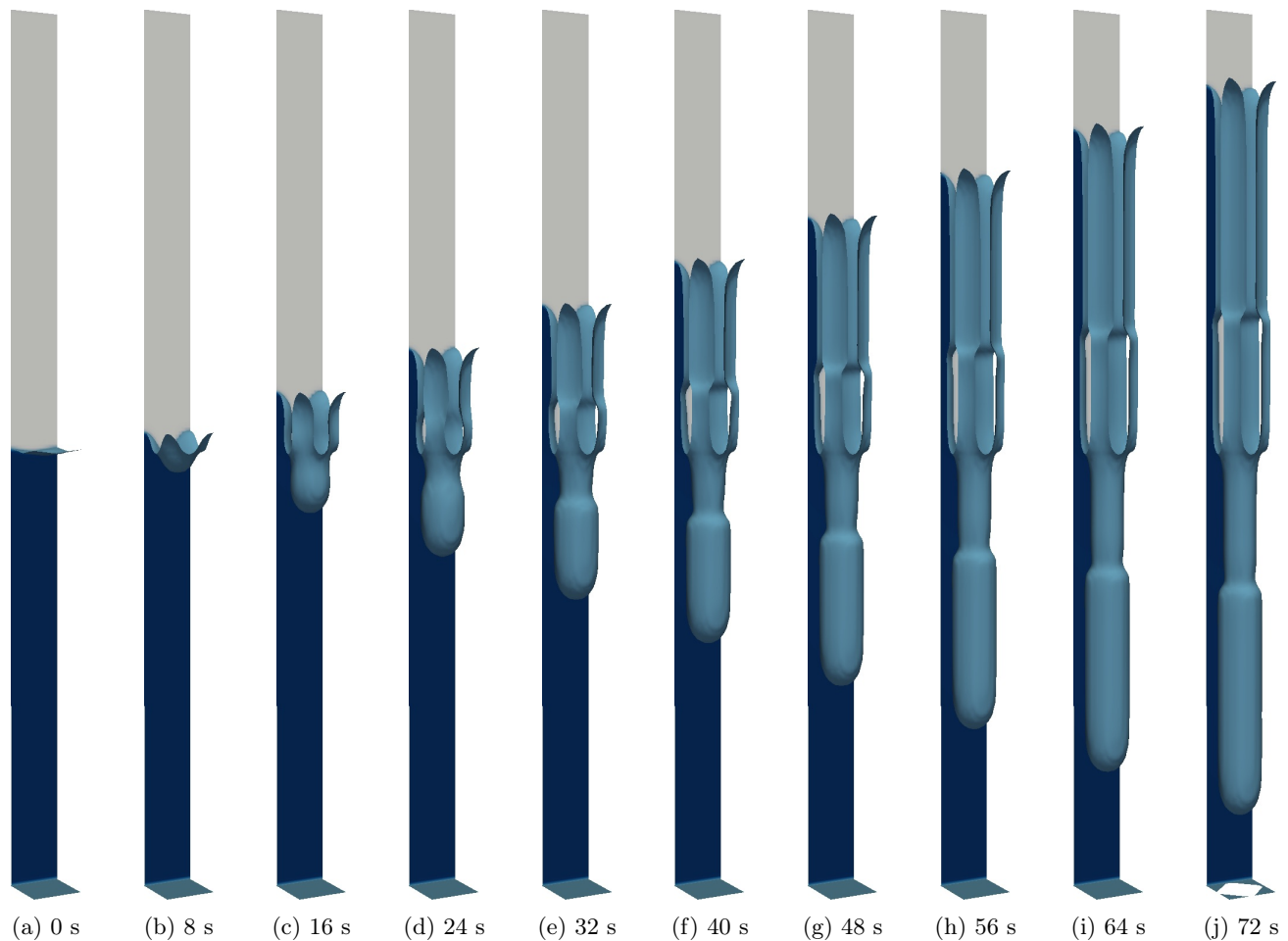


Figure 9: Evolution of the concentration field (dark blue: light fluid, light blue: heavy fluid) and of the interface during the evolution of the instability for $\lambda_0 \approx 1.76\lambda_c$ and $\eta = 2 \text{ Pa} \cdot \text{s}$ ($Re \approx 3$).

is approximately 3. From this picture (the snapshot are

taken at evenly spaced time), the velocity of the bubble tip seems to be constant.

In order to characterize the mass transport, we use the normalized flow rate Q/S where Q is defined by

$$Q = \max_{z \in [0, L_z]} \left(\int_{x=0}^{L_x} \int_{y=0}^{L_y} (v_z(1-c))(x, y, z) dx dy \right) \quad (37)$$

and $S = L_x \times L_y$ is the horizontal surface of the simulation domain. Q can be seen as the maximum of the flux of the light (resp. heavy) fluid through the horizontal planes of the domain, counted positively oriented toward the top (resp. the bottom). The previous observation is confirmed by the plots in Fig. 10 where both the normalized flow rate and the bubble tip speed are plotted as functions of time. It can be seen that, in this case, both quantities converge toward a steady state value after a short transient.

In Fig. 10, one can also see similar plots that were

obtained for the same wavelength $\lambda_0 \approx 1.76\lambda_c$ and different values of the viscosity. From these plots, the convergence toward a steady state is unclear for low values of the viscosity. Indeed, when η is decreased, one can see an alternation of acceleration and deceleration phases on the curve of Q/S . This regime is similar to damped oscillations and one may expect it to eventually converge toward a situation where Q/S is constant with time. However, for the lowest value of η , we observe a re-acceleration stage on the curve of v_b , as in Ref. 13 for instance, and a steady regime cannot establish itself. In the following, we will mostly limit ourselves to the configurations where a well defined steady regime is observed. We denote by v_b^{term} the terminal bubble velocity.

To better understand this regime, we first consider the evolution of the terminal bubble velocity as a function of

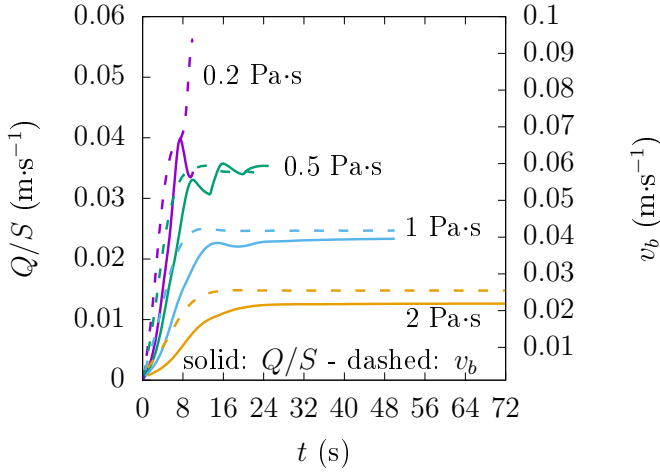


Figure 10: Q/S and v_b as a function of time for $\lambda_0 \approx 1.76\lambda_c$ and various η . For $\eta \geq 0.5 \text{ Pa} \cdot \text{s}$ ($3 \leq Re \leq 30$), after a short transient regime, a steady state is observed. For $\eta = 0.2 \text{ Pa} \cdot \text{s}$ ($Re \approx 90$), it is unclear if a steady regime will establish itself because v_b seems to re-increase.

the fluid viscosity. This evolution is presented in Fig. 11, for different values of the wavelength, and the bubble velocity is plotted as a function of $1/\eta$. For high values of η , i.e., small values of $1/\eta$, the bubble velocity is vanishing like $1/\eta$ as expected in the Stokes regime. As a matter of fact, it is straightforward from the Stokes equation in the permanent regime that the velocity is inversely proportional to η in this case. Let us recall that the Stokes velocity (velocity of a sphere falling in a viscous fluid) is proportional to $1/\eta$. And when η is further decreased, the bubble velocity increase is sublinear in $1/\eta$. In addition to the computational results, we present in Fig. 11 the theoretical prediction of Ref. 12 for the terminal velocity of the bubble in the case of a single-mode three-dimensional perturbation. With our notations, the formula translates into

$$v_b^{term} = -k_0 \frac{\eta}{\rho_2} + \sqrt{\frac{2A_t}{1+A_t} \frac{g}{k_0} - \frac{3k_0}{16} \frac{\gamma}{\rho_2} + k_0^2 \left(\frac{\eta}{\rho_2}\right)^2}, \quad (38)$$

where

$$A_t = \frac{\rho_2 - \rho_1}{\rho_1 + \rho_2} \quad (39)$$

is the Atwood number. Even though it is established for the case of an axisymmetric perturbation, one can see that it follows the computational results reasonably well in the considered range of parameters. Geometrical effects can explain the discrepancy between theory and numerics. A Taylor expansion applied to Eq. (38) shows that, when k_0 is fixed and $\eta \rightarrow \infty$,

$$v_b^{term} \approx \frac{\rho_2}{2k_0\eta} \left(\frac{2A_t}{1+A_t} \frac{g}{k_0} - \frac{3k_0}{16} \frac{\gamma}{\rho_2} \right) \quad (40)$$

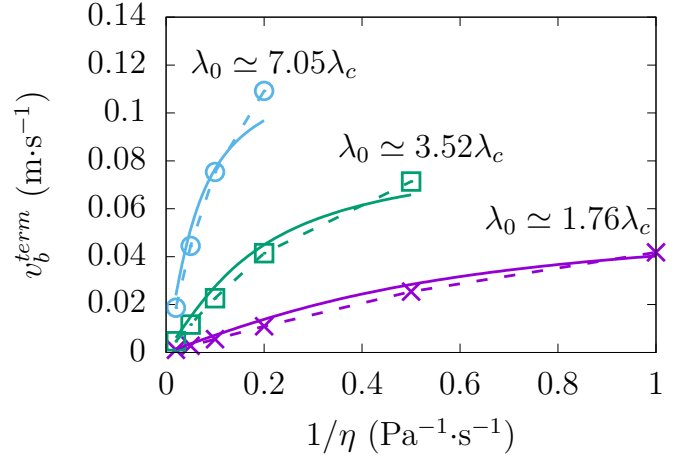


Figure 11: Bubble velocity in the steady regime as a function of the viscosity inverse for various values of the wavelength ($0.005 \leq Re \leq 20$). The symbols represent computational results. The dashed line is a guide for the eye. The solid line follows Eq. (38).

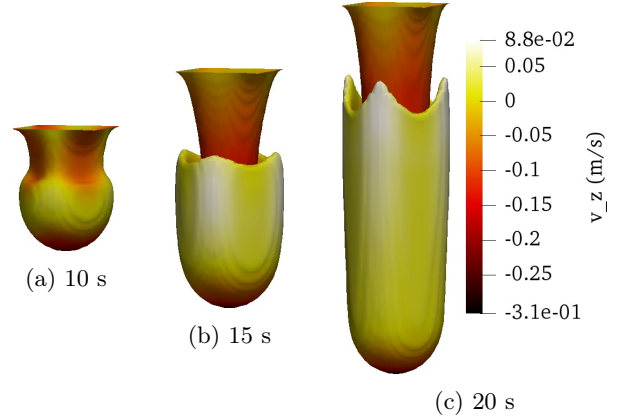


Figure 12: Typical pattern formed during the nonlinear stage of the instability at moderate Reynolds number (≈ 60). Evolution of the interface, in the bottom half of the domain, colored by the vertical velocity during the evolution of the instability for $\lambda_0 \approx 3.52\lambda_c$ and $\eta = 1 \text{ Pa} \cdot \text{s}$. One can see that boundary effects are present since the filament presents edges.

so that $v_b^{term} \propto 1/\eta$. This is consistent with the scaling of the velocity with $1/\eta$ observed in the simulations.

In the low η value cases, the flow is, as expected, reminiscent of what is observed in the case of perfect fluids, as can be seen in Fig. 12. In this figure, one can see that the flow organizes as follows: the heavy fluid is flowing *rapidly* downward in the central filament until it reaches the tip of the bubble. It then organizes as an almost cylindrical fluid sheet that is separated from the filament by a volume of light fluid. This fluid sheet is moving *slowly* upward or is almost at rest. This pattern persists over long time scales.

Finally, for the sake of completeness, we present in

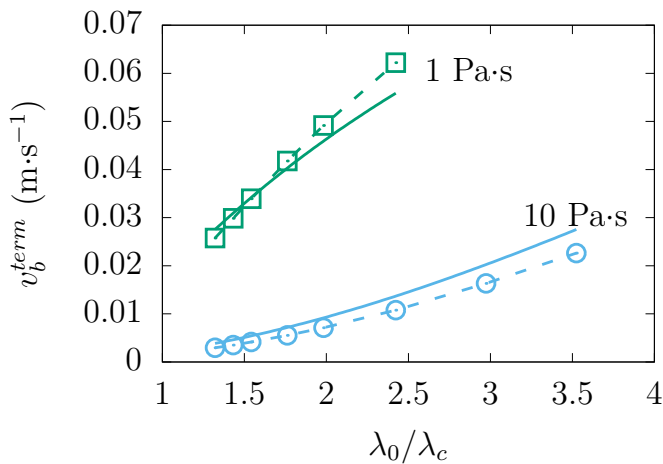


Figure 13: Bubble velocity in the steady regime as a function of the wavelength normalized by the critical wavelength for two viscosity values ($0.05 \leq Re \leq 20$).

The symbols represent computational results. The dashed line is a guide for the eye. The solid line follows Eq. (38).

Fig. 13, the terminal bubble velocity as a function of the wavelength normalized by the critical wavelength for two values of the viscosity. In both cases, the bubble velocity increases as a function of λ_0 . This is due to the fact that energy dissipation is higher at lower wavelength. Once again, the theoretical prediction of Ref. 12 follows the computational results reasonably well considering that it is not exactly based on the same initial perturbation.

VI. SUMMARY AND DISCUSSION

We have used the CHNS model to simulate the development of Rayleigh-Taylor instabilities in immiscible fluids with a low Atwood number and low-intermediate Reynolds numbers. The simulations were performed with a pseudo-spectral code. A first range of simulations was performed in two dimensions and at short time to capture the linear regime of the instability, in the case of inviscid or viscid fluids. Results show that this kind of diffuse-interface model is perfectly fit to capture this phenomenon, from a qualitative but also quantitative point of view. Even though the theory is based on a sharp-interface model, the numerical growth rates were very close to the theoretical ones (error of a few percents).

In addition, a careful convergence study has allowed us to elucidate the influence of the thermodynamic parameters on the convergence of the model. The accuracy of the CHNS model is limited by three main effects that are controlled by two parameters of the thermodynamic model: the interface thickness and the mobility. The interface thickness leads to quantitative errors that vanish linearly with the Cahn number w_{int}/L , where L is the characteristic lengthscale of the problem. By using a 1/100 ratio

approximately, we obtained errors of less than 5% on the growth rate of the instability. The effects of the mobility are more complex. The mobility is responsible for keeping the interface profile between the two fluids at thermodynamic equilibrium so that the source term in the flow equation correctly models the action of the surface tension with no overestimation. Hence, the mobility must be chosen high enough so that diffusion compensates flow effects at the scale of the interface thickness. Since the interface thickness is usually larger than the actual interface thickness in such models, diffusion is likely to be artificially overestimated. Such an overestimation can lead to inaccuracies if the diffusion fluxes lead to an interface motion that is not negligible. Hence, the mobility must be kept small enough to keep this motion negligible. As a result, the choice of the mobility is constrained by a balance between two opposite requirements: diffusion must be efficient at the scale of the interface thickness while it must be negligible at the macroscopic scale. In the case of the linear stability analysis, the inverse of the optimal Péclet number (determining the optimal mobility) was found to be proportional to the Cahn number, close to zero, which is in good agreement with former work²⁰.

A second range of simulations was performed in three dimensions and at long time to study the mass transport in the nonlinear regime. The study focused on low-intermediate Rayleigh number regimes. Single-mode perturbations with various wavelength were enforced initially. Results show that, when the inertial effects are negligible, a steady regime establishes itself. In this steady regime, the bubble tip velocity is constant. Its value depends linearly on the inverse of the viscosity and decreases when the wavelength of the perturbation is reduced. A reasonable agreement was found with a theoretical formula for axisymmetric perturbations.

From this study, we believe that we have provided a clear view of the CHNS model advantages and drawbacks in cases where a single lengthscale is present. It is simple to implement numerically and can handle without any additional cost topological changes of the phases. This comes at the expense of the need of resolving two length scales that must be separated by orders of magnitude in order to reach a good accuracy. It must also be noted that the choice of thermodynamic parameters is far from simple and must be made with care, taking into account the characteristic flow speed and lengthscale. In multiscale problems, the choice should be more involved. However, departures from the optimal Péclet number do not necessarily affect strongly the error (see Fig. 4b). In this case, using an intermediate lengthscale of the problem as reference should prove reasonable. Let us finally remark that, in the case of turbulent flows, the model will not be able to describe the smaller length scales at which the energy dissipation occurs and that this may affect the convergence of the model.

Appendix A: Growth rate of the Rayleigh-Taylor instability in viscous fluids

Introducing a dimensionless wavenumber, growth rate and surface tension,

$$k^* = \left(\frac{\nu_m^2}{A_t g} \right)^{\frac{1}{3}} k, \quad \alpha^* = \left(\frac{\nu_m}{A_t^2 g^2} \right)^{\frac{1}{3}} \alpha$$

and $\gamma^* = \left(\frac{1}{A_t g \nu_m^4 (\rho_1 + \rho_2)^3} \right)^{\frac{1}{3}} \gamma,$ (A1)

where ν_m is a mean kinematic viscosity defined by

$$\nu_m = \frac{\eta_1 + \eta_2}{\rho_1 + \rho_2}, \quad (\text{A2})$$

the authors of Ref. 5 claim that the ratio $s = \alpha^*/(k^*)^2$ is root of the equation

$$s^2 + 2sH(s) = R, \quad (\text{A3})$$

where

$$H(s) = \frac{2a(s)b(s)}{a(s) + b(s)}, \quad (\text{A4})$$

$$a(s) = C_2 + \sqrt{C_1 + C_1 A_1 s},$$

$$b(s) = C_1 + \sqrt{C_2 + C_2 A_2 s}, \quad (\text{A5})$$

$$A_i = \frac{\rho_i}{\rho_1 + \rho_2}, \quad C_i = \frac{\eta_i}{\eta_1 + \eta_2}, \quad i = 1, 2, \quad (\text{A6})$$

and

$$R = \frac{1 - \gamma^*(k^*)^2}{(k^*)^3}. \quad (\text{A7})$$

We compute an estimate of this root by using Newton's method.

ACKNOWLEDGMENTS

This work was supported by the CEA (Commissariat à l'énergie atomique et aux énergies alternatives) and EDF (Electricité de France). The computations were performed on the clusters of Ecole Polytechnique and GENCI-IDRIS (project 0042B07727). We thank Mathis Plapp from PMC Laboratory for the valuable discussions.

DATA AVAILABILITY STATEMENT

The data that support the findings of this study are available from the corresponding author upon reasonable request.

REFERENCES

- ¹D. H. Sharp, "An overview of Rayleigh-Taylor instability," *Physica 12D*, 3–18 (1984).
- ²Y. Zhou, "Rayleigh–Taylor and Richtmyer–Meshkov instability induced flow, turbulence, and mixing. I," *Physics Reports* **720–722**, 1–136 (2017).
- ³G. Taylor, "The instability of liquid surfaces when accelerated in a direction perpendicular to their planes. I," *Proc. R. Soc. Lond. A* **201**, 192–196 (1950).
- ⁴S. Chandrasekhar, *Hydrodynamic and Hydromagnetic Stability* (Clarendon Press, 1961).
- ⁵R. Menikoff, R. C. Mjolsness, D. H. Sharp, and C. Zemach, "Unstable normal mode for Rayleigh–Taylor instability in viscous fluids," *Phys. Fluids* **20**, 2000–2004 (1977).
- ⁶D. J. Lewis and G. Taylor, "The instability of liquid surfaces when accelerated in a direction perpendicular to their planes. II," *Proc. R. Soc. Lond. A* **202**, 81–96 (1950).
- ⁷J. T. Waddell, C. E. Niederhaus, and J. W. Jacobs, "Experimental study of Rayleigh–Taylor instability: Low Atwood number liquid systems with single-mode initial perturbations," *Phys. Fluids* **13**, 1263–1273 (2001).
- ⁸J. P. Wilkinson and J. W. Jacobs, "Experimental study of the single-mode three-dimensional Rayleigh-Taylor instability," *Phys. Fluids* **19**, 124102 (2007).
- ⁹D. Oron, L. Arazi, D. Kartoon, A. Rikanati, U. Alon, and D. Shvarts, "Dimensionality dependence of the Rayleigh–Taylor and Richtmyer–Meshkov instability late-time scaling laws," *Phys. Plasmas* **8**, 2883–2889 (2001).
- ¹⁰V. N. Goncharov, "Analytical Model of Nonlinear, Single-Mode, Classical Rayleigh-Taylor Instability at Arbitrary Atwood Numbers," *Phys. Rev. Lett.* **88**, 134502 (2002).
- ¹¹Y.-N. Young and F. E. Ham, "Surface tension in incompressible Rayleigh-Taylor mixing flow," *J. Turbulence* **7**, 1–23 (2006).
- ¹²S.-I. Sohn, "Effects of surface tension and viscosity on the growth rates of Rayleigh-Taylor and Richtmyer-Meshkov instabilities," *Phys. Rev. E* **80**, 055302 (2009).
- ¹³P. Ramaprabhu, G. Dimonte, Y.-N. Young, A. C. Calder, and B. Fryxell, "Limits of the potential flow approach to the single-mode Rayleigh-Taylor problem," *Phys. Rev. E* **74**, 066308 (2006).
- ¹⁴T. Wei and D. Livescu, "Late-time quadratic growth in single-mode Rayleigh-Taylor instability," *Phys. Rev. E* **86**, 046405 (2012).
- ¹⁵P. Ramaprabhu, G. Dimonte, P. Woodward, C. Fryer, G. Rockefeller, K. Muthuraman, P.-H. Lin, and J. Jayaraj, "The late-time dynamics of the single-mode Rayleigh-Taylor instability," *Phys. Fluids* **24**, 074107 (2012).
- ¹⁶Z.-X. Hu, Y.-S. Zhang, B. Tian, Z. He, and L. Li, "Effect of viscosity on two-dimensional single-mode Rayleigh-Taylor instability during and after the reacceleration stage," *Phys. Fluids* **31**, 104108 (2019).
- ¹⁷D. M. Anderson, G. B. McFadden, and A. A. Wheeler, "Diffuse-interface methods in fluid mechanics," *Annu. Rev. Fluid Mech.* **30**, 139–165 (1998).
- ¹⁸J. W. Cahn and J. E. Hilliard, "Free Energy of a Nonuniform System. I. Interfacial Free Energy," *J. Chem. Phys.* **28**, 258–267 (1958).
- ¹⁹J. W. Cahn, "Phase Separation by Spinodal Decomposition in Isotropic Systems," *J. Chem. Phys.* **42**, 93–99 (1965).
- ²⁰F. Magaletti, F. Picano, M. Chinappi, L. Marino, and C. M. Casciola, "The sharp-interface limit of the Cahn-Hilliard/Navier-Stokes model for binary fluids," *J. Fluid Mech.* **714**, 95–126 (2013).
- ²¹A. Celani, A. Mazzino, P. Muratore-Ginanneschi, and L. Vozella, "Phase-field model for the Rayleigh-Taylor instability of immiscible fluids," *J. Fluid Mech.* **622**, 115–134 (2009).
- ²²H. G. Lee, K. Kim, and J. Kim, "On the long time simulation of the Rayleigh–Taylor instability," *Int. J. Numer. Meth. Engng* **85**, 1633–1647 (2011).

- ²³H. G. Lee and J. Kim, “Numerical simulation of the three-dimensional Rayleigh-Taylor instability,” *Computer and Mathematics with Applications* **66**, 1466–1474 (2013).
- ²⁴L. Hong, H. Xiaoliang, H. Xuefeng, and X. Jiangrong, “Direct numerical simulations of multi-mode immiscible Rayleigh-Taylor instability with high Reynolds numbers,” *Phys. Fluids* **31**, 112104 (2019).
- ²⁵I. Nitschke, A. Voigt, and J. Wensch, “A finite element approach to incompressible two-phase flow on manifolds,” *J. Fluid Mech.* **708**, 418–438 (2012).
- ²⁶Q. Yang, B. Q. Li, Z. Zhao, J. Shao, and F. Xu, “Numerical analysis of the Rayleigh-Taylor instability in an electric field,” *J. Fluid Mech.* **792**, 397–434 (2016).
- ²⁷T. Lyubimova, A. Vorobev, and S. Prokopev, “Rayleigh-Taylor instability of a miscible interface in a confined domain,” *Phys. Fluids* **31**, 014104 (2019).
- ²⁸B. Song, C. Plana, J. M. Lopez, and M. Avila, “Phase-field simulation of core-annular pipe flow,” *Int. J. Multiphase Flow* **117**, 14–24 (2019).
- ²⁹V. M. Kendon, M. E. Cates, J.-C. Desplat, I. Pagonabarraga, and P. Bladon, “Inertial effects in three dimensional spinodal decomposition of a symmetric binary fluid mixture: A lattice Boltzmann study,” *J. Fluid Mech.* **440**, 147–203 (2001).
- ³⁰H. Henry and G. Tegze, “Self-similarity and coarsening rate of a convecting bicontinuous phase separating mixture : Effect of the viscosity contrast,” *Phys. Rev. F* **3**, 074306 (2018).
- ³¹H. Henry and G. Tegze, “Kinetics of coarsening have dramatic effects on the microstructure : Self-similarity breakdown induced by viscosity contrast,” *Phys. Rev. E* **100**, 013116 (2019).